© 2019. Published by The Company of Biologists Ltd | Journal of Cell Science (2019) 132, jcs228999. doi:10.1242/jcs.228999

RESEARCH ARTICLE

Dynamic label-free imaging of lipid droplets and their link to fatty acid and pyruvate oxidation in mouse eggs

Josephine Bradley[1], Iestyn Pope[1], Yisu Wang[1], Wolfgang Langbein[2], Paola Borri[1] and Karl Swann[1,*]

ABSTRACT

Mammalian eggs generate most of their ATP by mitochondrial oxidation of pyruvate from the surrounding medium or from fatty acids that are stored as triacylglycerols within lipid droplets. The balance between pyruvate and fatty acid oxidation in generating ATP is not established. We have combined coherent anti-Stokes Raman scattering (CARS) imaging with deuterium labelling of oleic acid to monitor turnover of fatty acids within lipid droplets of living mouse eggs. We found that loss of labelled oleic acid is promoted by pyruvate removal but minimised when β-oxidation is inhibited. Pyruvate removal also causes a significant dispersion of lipid droplets, while inhibition of β-oxidation causes droplet clustering. Live imaging of luciferase or FAD autofluorescence from mitochondria, suggest that inhibition of β-oxidation in mouse eggs only leads to a transient decrease in ATP because there is compensatory uptake of pyruvate into mitochondria. Inhibition of pyruvate uptake followed by β-oxidation caused a similar and successive decline in ATP. Our data suggest that β-oxidation and pyruvate oxidation contribute almost equally to resting ATP production in resting mouse eggs and that reorganisation of lipid droplets occurs in response to metabolic demand.

KEY WORDS: Egg, CARS, β-oxidation, Lipid droplets, Deuterated lipids

INTRODUCTION

Ovulated mouse eggs (metaphase II-arrested oocytes; hereafter referred to as MII eggs) depend almost entirely upon their ∼100,000 mitochondria for ATP production through oxidative phosphorylation (Dumollard et al., 2004). Mitochondria continue to supply most ATP during the early cleavage divisions because glycolytic activity is low in mammalian embryos until the morula or blastocyst stages (Downs, 1995). Substrates, such as pyruvate and fatty acids, are taken up into and oxidised within the mitochondria. Pyruvate is provided by the follicular fluid and glycolytic cumulus cells surrounding the developing egg within the ovarian follicle (Downs, 1995), while *in vitro*, pyruvate is supplemented within the culture medium.

Fatty acids are also taken up into the egg from the follicular fluid and may reside as free fatty acids within the cytosol, or they are densely stored as triacylglycerols (TAGs) within vesicles known as lipid droplets (LDs) (Homa et al., 1986). The composition of LDs seems to be similar between different species (Bradley, 2016; McEvoy et al., 2000). Although it is well established that mammalian eggs oxidise both pyruvate and fatty acids, the balance between these substrates is unclear. Some species, such as pigs, dogs and cows, have a substantial amount of lipid in the form of large LDs in their cytoplasm, which gives them a dark appearance under optical transmission microscopy (Sturmey and Leese, 2003; Apparicio et al., 2012). In contrast, mouse and human eggs have a more-transparent cytoplasm that, for mouse eggs, is clearly associated with a much reduced lipid content (Bradley et al., 2016).

Pyruvate is the primary essential energy source for developing mouse and human eggs/embryos (Gardner and Leese, 1986). Starving mouse eggs of pyruvate by using mitochondrial uptake inhibitors, such as cinnamate derivatives, greatly affects the developmental potential of the egg (Dumollard et al., 2007). Luminescence imaging of ATP levels by using injected firefly luciferase has been used to show that eggs deprived of substrates exhibit reduced ATP and that only pyruvate – and not glucose, glutamine or lactate – can restore ATP levels (Dumollard et al., 2008). Pyruvate uptake and the stimulation of egg mitochondrial metabolism can also be specifically monitored by measuring the flavin adenine dinucleotide (FAD) autofluorescence (green) (Dumollard et al., 2004). FAD is bound to flavoproteins in the mitochondria and the FAD:$FADH_2$ ratio reflects the redox state of mitochondria (Dumollard et al., 2004). Both luciferase imaging of ATP and autofluorescence imaging of FAD have been used to demonstrate Ca^{2+}-induced increases in $FADH_2$ and ATP production in mouse egg mitochondria during the Ca^{2+} oscillations at fertilisation (Dumollard et al., 2004). These methods have, thus far, not been used to investigate lipid metabolism in mouse eggs.

Despite the recognised role of pyruvate metabolism in supporting mouse embryo development, it has become clear that fatty acid oxidation is also significant. Dunning et al. showed that mouse embryos metabolise palmitic acid and that the promotion of β-oxidation by using L-carnitine to facilitate fatty acid transport into mitochondria resulted in increased egg quality, fertilisation and blastocyst rates (Dunning et al., 2011). The same group also demonstrated that β-oxidation inhibition following application of the mitochondrial uptake inhibitor Etomoxir, impairs blastocyst development (Dunning et al., 2010). Hence, mitochondrial fatty acid oxidation may also contribute to energy production in mouse eggs and early embryos, despite their low lipid content. However, it is not clear what fraction of ATP production might originate from fatty acid β-oxidation. It is also not known whether fatty acid oxidation utilises fatty acid derived from endogenous LDs or exogenous sources. One limitation is that real-time imaging methods used to investigate LD and fatty acid metabolism in eggs and embryos are less well-developed compared with those monitoring cytosolic or mitochondrial redox state, or ATP production. Destructive chemical analysis of lipids does not allow for the assessment of spatial and dynamic events.

[1]School of Biosciences, Cardiff University, The Sir Martin Evans Building, Museum Avenue, Cardiff, CF10 3AX. [2]School of Physics and Astronomy, Cardiff University, The Parade, Cardiff, CF24 3AA.

*Author for correspondence (SwannK1@cardiff.ac.uk)

Y.W., 0000-0001-9052-2184; K.S., 0000-0002-4355-1449

Received 4 January 2019; Accepted 28 May 2019

Journal of Cell Science (2019) 132, jcs228999. doi:10.1242/jcs.228999

We have previously demonstrated the use of coherent anti-Stokes Raman scattering (CARS) microscopy to quantify number, spatial distribution and chemical content of LDs, in mouse eggs and embryos without compromising the viability of the egg (Bradley et al., 2016). CARS microscopy is label-free and chemically specific (Potma and Xie, 2004). It is based on the phenomenon of Raman scattering, namely the interaction of light with vibrating chemical bonds, yielding light scattered at a different wavelength (hence the colour) compared to the incident light. The shift in wavelength is a direct signature of the frequency of the vibration that, in turn, depends on the type of chemical bond. Although this scattering phenomenon usually produces a very weak signal, it can be enhanced when two short laser pulses are used to coherently drive the vibrations. This way, the scattered light from all bonds of the same type in the focal volume interferes constructively, generating CARS that can be acquired at high speed for chemically specific live cell imaging applications. CARS is very effective when imaging lipids since lipids contain a large number of identical CH_2 bonds in the aliphatic chain, and lipid molecules are densely packed inside LDs. CARS also provides intrinsic three-dimensional spatial resolution without the need of a confocal detection pin-hole, as the nonlinear process only takes place within the focal volume, where high photon densities are reached. Previously, we have quantified number, size and aggregation patterns of LDs within the cytoplasm of live mouse eggs (Bradley et al., 2016). The amplitude of the CARS signal from each droplet also allowed us to assess the total lipid content, as the number of CH_2 bonds within the focal volume is proportional to the square root of the CARS intensity. CARS imaging of eggs and early embryos at the CH_2 vibrational resonance, i.e. 2850 cm^{-1}, showed that LD distribution and size changed as development continued. Immature Germinal vesicle (GV) eggs, i.e. immature oocytes prior to meiosis, displayed LDs spatially dispersed throughout the cytoplasm, whereas LDs in mature MII eggs exhibited a more 'clustered' configuration, i.e. LD aggregates. These studies show that CARS imaging can be used to characterise LD spatial patterns and lipid content, in live eggs and embryos.

As well as probing the CH_2 vibrational resonance, CARS microscopy can be used to excite and monitor carbon-deuterium (C-D) bonds (Potma and Xie, 2004; Bergner et al., 2011). Owing to the heavier isotopic mass, deuterated bonds have a lower vibrational resonance compared to their hydrogen counterpart, providing a recognisable CARS signal in the frequency range 2000 cm^{-1} to 2600 cm^{-1}. This was first demonstrated by Duncan et al. with the detection of the deuterium-oxygen bond (D-O) in deuterated water (D_2O, also referred to as heavy water) with a CARS peak at a frequency of 2450 cm^{-1} (Duncan et al. 1982). For lipids, the CD_2 symmetric stretch vibration has a CARS peak at 2140 cm^{-1}, distinctly separated from non-deuterated CH_2 that has a CARS peak at 2850 cm^{-1}. Notably, the CD_2 CARS peak is also distinct from those arising due to the vibrational resonances from other cellular components, and lies within the otherwise 'silent' region of the CH_2 lipid Raman spectral profile (see Fig. 1). Thus, deuterium-labelled lipids can be selectively imaged with CARS, well-separated from naturally-occurring lipids within cells (Rodriguez et al., 2006). Deuterated palmitic acid has previously been shown by using stimulated Raman spectroscopy (SRS) to be taken up into LDs within CHO cells and whole nematodes (Zhang et al., 2011; Fu et al., 2014) but experimental investigation of the turnover of labelled fatty acids has not been carried out.

In this paper, we use CARS microscopy to investigate how the LD spatial distribution in mouse eggs relates to the extent of mitochondrial metabolism occurring within the cell. We find that starving eggs of pyruvate leads to a wide dispersion of LDs, whereas inhibition of β-oxidation leads to an increased clustering of LDs. We employ deuterated-oleic acid (DOA) to specifically and unambiguously assess the storage and use of fatty acids within the mammalian egg. We show how the rate loss of deuterium labelling of LDs is increased by removal of pyruvate as a substrate, while inhibition of β-oxidation maintains the amount of DOA within the egg. Using live cell imaging of luciferase luminescence, we find that inhibition of β-oxidation only leads to a transient decrease in ATP levels. Using the autofluorescence of FAD, we then show that inhibition of fatty acid oxidation leads to an unexpected decrease in FAD (increase in $FADH_2$). This is likely to be due to compensatory uptake of pyruvate, which could explain why ATP levels are restored in the absence of β-oxidation. Our data suggest that β-oxidation contributes ∼50% of the mitochondrial ATP production in eggs and that this is in dynamic balance with pyruvate oxidation.

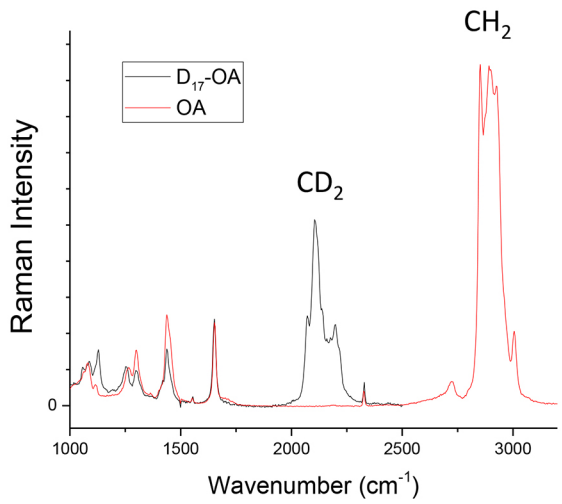

Fig. 1. Raman spectra of deuterated and non-deuterated OA. Raman spectra showing the vibrational resonances of the CD_2 bond in deuterated OA (D_{17}-OA) at ∼2100 cm^{-1} and of the CH_2 bond in non-deuterated OA (OA) at 2850 cm^{-1}. The CD_2 bond lies in the silent region of the spectrum, where no vibrational modes are present for the non-deuterated compound, allowing for its distinct detection.

RESULTS

Lipid droplet distribution reflects metabolic state

As we have shown previously (Bradley et al., 2016), CARS microscopy at the CH_2 symmetric stretch vibration (2850 cm^{-1}), abundant in the acyl chain of fatty acids, allows label-free chemically specific imaging of lipid droplets in live cells. LDs in MII eggs cultured in simple M2 medium present a spatial distribution of multiple small clusters throughout the cell cytoplasm (Fig. 2D). It is notable that these clusters are also apparent in high-resolution differential interference contrast (DIC) images (Fig. 2A) and can be chemically identified by using CARS microscopy. Starving MII eggs of carbohydrate and glutamine in response to incubation in HKSOM lacking pyruvate, lactate, glutamine and glucose for ∼6 h prior to CARS imaging, led to wide spatial dispersion of LDs throughout the whole egg (Fig. 2E). This is also identifiable through the lack of clusters seen by using high-resolution DIC (Fig. 2B). In contrast, inhibition of β-oxidation with 100 µM Etomoxir for ∼6 h prior to CARS imaging, causes an LD distribution somewhat exaggerated from the norm, appearing to have an increased number and size of LD clusters (Fig. 2F). Again, these changes are also apparent in images taken with DIC (Fig. 2C).

Journal of Cell Science (2019) 132, jcs228999. doi:10.1242/jcs.228999

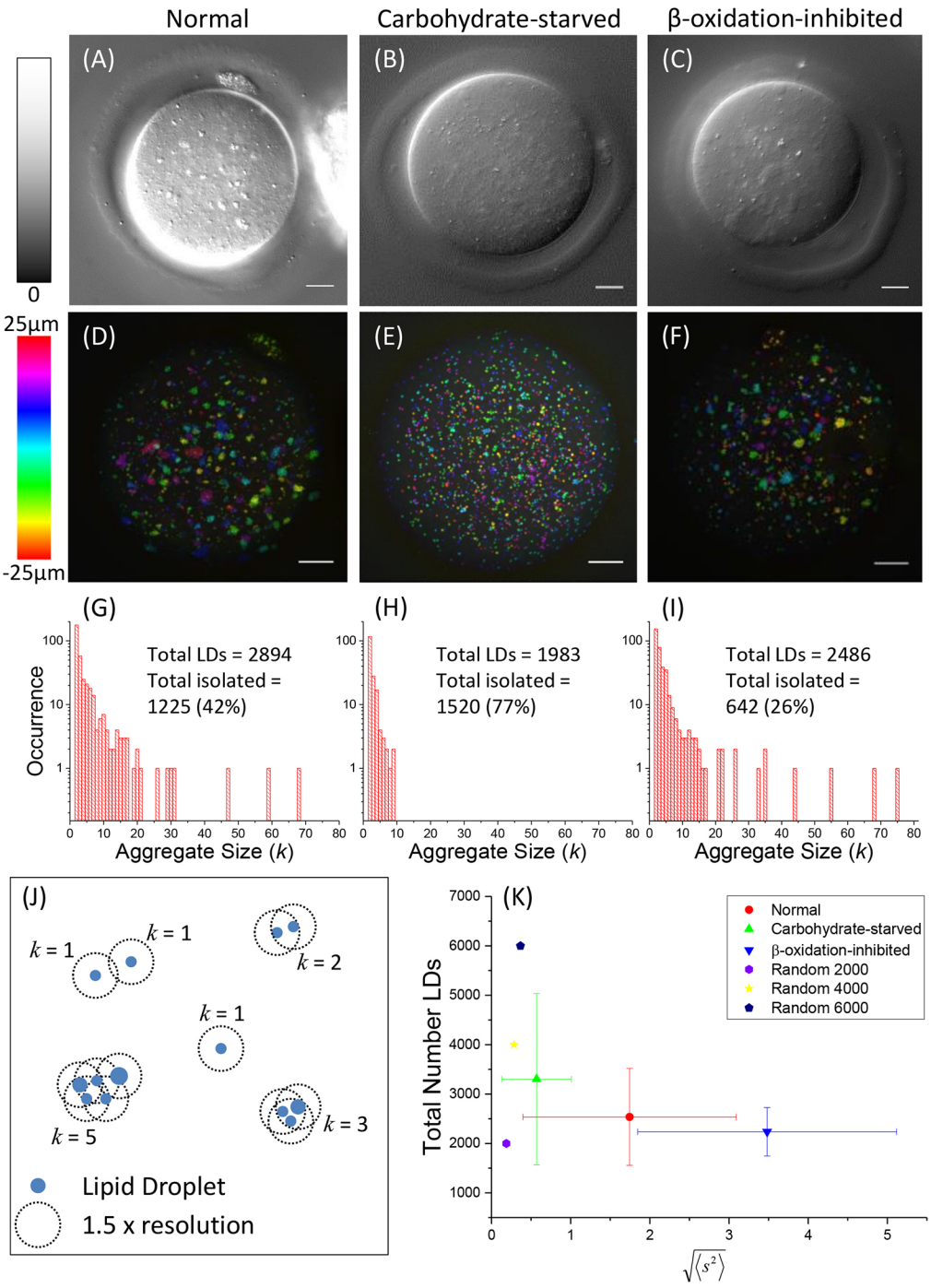

Fig. 2. Lipid droplet aggregation patterns in MII eggs with altered mitochondrial metabolism. (A,D,G) MII egg incubated in simple M2 medium (*n*=30). (B,E,H) Carbohydrate-starved MII egg (*n*=8). (C,F,I) β-Oxidation-inhibited MII egg (100 µM Etomoxir) (*n*=6). (A-C) Single-plane (approximately equatorial) DIC images using a 1.27 NA water objective and a 0.72 NA dry condenser. (D-F) Images show depth colour-coded CARS *z*-stacks at wavenumber 2850 cm^{-1} (CH_2 vibration) through the same MII eggs. *xy* pixel size, 0.1×0.1 µm; *z*-step, 0.5 µm; pixel dwell time, 0.01 ms; Pump (Stokes) power at the sample, ~14 mW (~9 mW). Scale bars: 10 µm; colour bar shows depth of colour coding, ranging from −25 µm to +25 µm, of 101 *z*-stacks, with 0 µm being the approximate equatorial plane of the egg. The brightness of each colour is the maximum intensity at each corresponding *z*-plane. (G-I) Representative histograms of the number of LDs making up clusters for the different growth conditions above. (J) Cartoon illustrating the determination of LD cluster size. (K) Scatter plot of the square root of the mean squared cluster size ($\sqrt{\langle s^2 \rangle}$) against the total number of LDs. The aggregation pattern of 2000, 4000 and 6000 random droplets is also shown. The distribution of each variable in the corresponding ensemble is shown as the average ±s.d. Data represent multiple trials, using two to three mice per trial.

Quantitative analysis of the aggregate patterns within these eggs was performed as described by Bradley et al. (2016). Briefly, an LD was considered being part of a ‘cluster’ when the LD centre spatial position was within a distance of 1.5×the resolution (0.3 µm laterally, 0.6 µm axially) to that of the nearest neighbouring droplet (Fig. 2J). Each droplet determined to be within the same cluster was given the same index value. The occurrence of such index was then used to count the number of LDs in one cluster, in order to obtain the cluster – or aggregate – ‘size’. The occurrence of aggregate sizes was then obtained, as shown in the histograms in Fig. 2G-I. MII eggs demonstrate numerous clusters above size 10, i.e. comprising more than ten LDs, with only 59.5±14.4% (mean±s.d.) of LDs in a non-clustered, isolated position (Fig. 2G). Carbohydrate starvation led to the total lack of clusters above size 10, with 84.1±10.8% of LDs isolated (Fig. 2H). Inhibition of β-oxidation causes LDs to aggregate into more clusters of bigger size (i.e. higher numbers of LDs than typically seen in a normal MII egg), with only 38.4±14.9% isolated LDs (Fig. 2I). The extent of LD aggregation was calculated as the square root of the mean square aggregate size ($\sqrt{\langle s^2 \rangle}$) per egg (see Materials and Methods) and followed by plotting the average $\sqrt{\langle s^2 \rangle}$ per population of eggs at each condition (see Fig. 2K). This analysis confirms that significantly fewer clusters are seen in a carbohydrate-starved egg (green triangle, Fig. 2K), compared to an egg subjected to inhibition of β-oxidation (blue inverted triangle, Fig. 2K). Normal MII (red circle, Fig. 2K) and β-oxidation-inhibited MII LD distributions are seen to be

Journal of Cell Science (2019) 132, jcs228999. doi:10.1242/jcs.228999

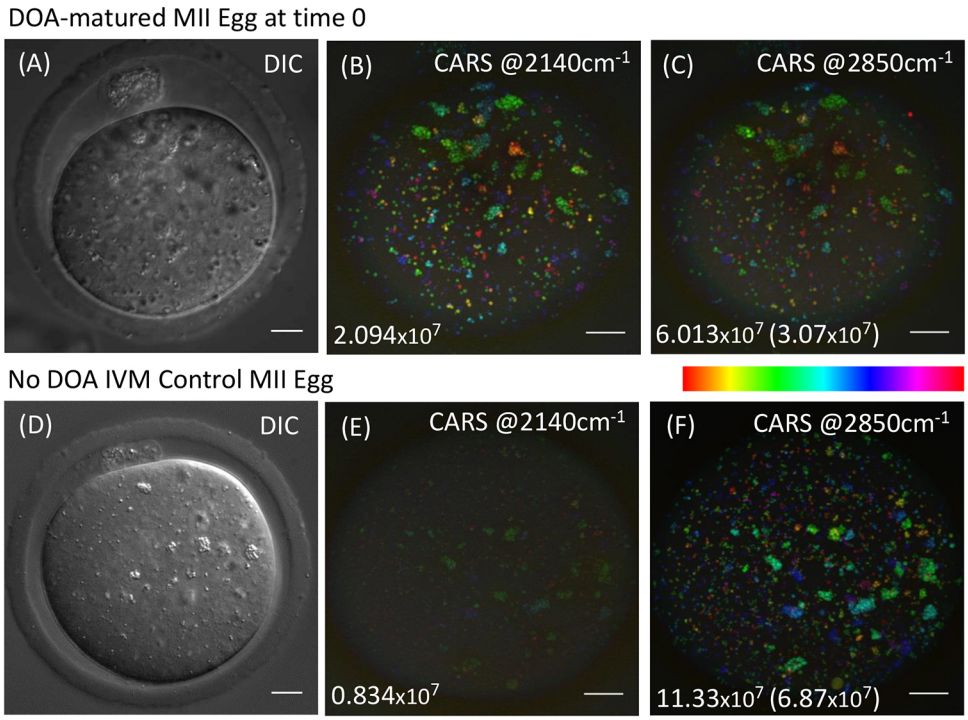

Fig. 3. CARS imaging of eggs incubated with DOA. (A,D) Single-plane (approximately equatorial) DIC images using a 1.27 NA water objective and a 0.72 NA dry condenser. (B,C,E,F) Images show depth colour-coded CARS *z*-stacks at wavenumbers 2140 cm^{-1} (CD_2 vibration) and 2850 cm^{-1} (CH_2 vibration) through the same MII eggs, showing DOA in LDs. MII egg *in vitro* matured with 400 µM DOA (*n*=5; A-C), control MII egg *in vitro* matured without DOA (*n*=3; D-F). Maximum CARS intensities are shown in photoelectrons per second (ph.e^{-}/s). Values in parenthesis in C and F denote the intensity under excitation conditions identical to those in B and E, respectively, i.e. they are corrected for the varying temporal overlap of pump and Stokes at different wavenumbers. Depth colour-coded CARS images shown in B and E were adjusted to the brightness of that shown in B; depth colour-coded CARS images shown in C and F were adjusted to the brightness of that shown in F. *xy* pixel size, 0.1×0.1 µm; *z*-step, 0.5 µm; pixel dwell time, 0.01 ms; Pump (Stokes) power at the sample, ~14 mW (~9 mW). Scale bars: 10 µm. Colour bar shows depth of colour coding, ranging from −25 µm to 25 µm, of 101 *z*-stacks, with 0 µm being the approximate equatorial plane of the egg. Data represent multiple trials, using two to three mice per trial.

different from a random distribution of LDs. This is exemplified in Fig. 2K (violet hexagon, yellow star, dark blue pentagon), where we calculated the occurrence of LD clusters and, in turn, $\sqrt{\langle s^2 \rangle}$, by simulating a completely random distribution of 2000, 4000 or 6000 droplets within the same egg volume. These data suggest that the degree of LD clustering reflects whether carbohydrates or fatty acids are being oxidised by mitochondria.

Dynamic imaging of endogenous fatty acid turnover

Mouse eggs can survive and maintain some ATP production for many hours in media without carbohydrates (Dumollard et al., 2004, 2008). This implies that mitochondria metabolise endogenous substrates, such as fatty acids, stored in LDs. We sought to monitor this by using deuterated lipids. CD_2 is abundant in deuterated fatty acids and gives rise to a resonant CARS intensity frequency that is shifted from the CH_2 stretch vibration (Fig. 1). Therefore, deuterated fatty acids can be used as a non-invasive 'label' for CARS imaging, in order to examine how specific fatty acids are stored into LDs or metabolised from them. Notably, from the CARS intensity strength, we can quantitatively examine whether deuterated fatty acid accumulation is gained with incubation or lost with metabolism.

GV oocytes were *in vitro* matured in maturation medium containing 400 µM DOA. CARS imaging of the resulting MII eggs at the CD_2 vibration (2140 cm^{-1}) and the CH_2 vibration (2850 cm^{-1}) peaks clearly demonstrates that DOA is taken up into the cell from the surrounding medium during maturation; it is stored as TAGs within LDs, providing a high CARS intensity (Fig. 3B and Table 1), albeit lower than the signal intensity from non-deuterated fatty acids at the CH_2 peak (Fig. 3C and Table 1). Uptake was further demonstrated by comparing a DOA-matured egg with a control egg

Table 1. CARS maximum intensity and mean DOA volume per LD (v) of *in vitro* mouse eggs with altered mitochondrial metabolism

Imaged mouse eggs	CD_2 signal at 2140 cm^{-1} (×10^7 ph.e^{-}/s)	CH_2 signal at 2850 cm^{-1} (×10^7 ph.e^{-}/s, corrected*)	Mean DOA volume per LD (*v*) ±s.e.m. (µm^3×10^{-2})
Control 1 without DOA (*t*=0)	0.83	6.87	0.45±0.04
Control 2 +DOA (*t*=0)	2.09	3.07	5.3±2.7
+DOA prior to M2 only (*t*=6 h)	1.05	2.78	2.0±1.2
+DOA prior to carbohydrate starvation (*t*=6 h)	0.65	1.21	0.31±0.08
+DOA prior inhibition of β-oxidation (*t*=6 h)	1.74	3.81	3.6±1.0

Control 1, incubation in M2 medium without DOA; **Control 2**, incubation in M2 medium+DOA; **Carbohydrate starvation**, incubation in HKSOM (lacking pyruvate, lactate, glutamine, glucose); **Inhibition of β-oxidation**, incubation in M2 medium +Etomoxir.
+DOA, 18-h incubation in M2 medium supplemented with 400 µM DOA; *t*, time of imaging after incubation; *, see Materials and Methods,

Journal of Cell Science (2019) 132, jcs228999. doi:10.1242/jcs.228999

matured *in vitro* without DOA (Fig. 3E and Table 1). Imaging at the CD_2 vibrational mode in an MII egg matured without DOA showed that the control egg provides decreased CARS intensity (albeit not zero, due to the non-resonant CARS contribution) compared with a DOA-incubated egg, whereas CARS intensity at the CH_2 peak within the same egg (Fig. 3F and Table 1) was considerably higher. Examples of CARS spectra of individual LDs acquired by using the hyperspectral imaging modality available with the microscope (Pope et al., 2013) showed the CD_2 vibrational peak alongside the CH_2 stretching band that is characteristic of lipids (Fig. S1). These data show that CARS imaging can detect DOA taken up by LDs in live mouse eggs.

Extended culture of DOA-matured eggs in M2 medium for ∼6 h allowed us to see the loss of DOA label over time and, thus, the physiological turnover of fatty acids within the egg. Fig. 4B shows that the CARS signal intensity at the CD_2 peak [1.05×10^7 photoelectrons (ph.e$^-$)/s] was roughly half of that of an MII egg immediately after maturation in the presence of DOA (time 0; 2.09×10^7 ph.e$^-$/s; Fig. 3B). Although the CARS signal at the CH_2 peak remains higher than at CD_2 (2.78×10^7 ph.e$^-$/s; Fig. 4C), the signal is still lower than seen for CH_2 at time 0 (3.07×10^7 ph.e$^-$/s; Fig. 3C). Incubation of DOA-matured eggs alongside carbohydrate-starvation for ∼6 h before CARS imaging leads to the exaggerated loss of CARS signal at both the CD_2 (0.65×10^7 ph.e$^-$/s; Fig. 4E) and CH_2 peaks (1.21×10^7 ph.e$^-$/s; Fig. 4F). The loss of DOA appears to be in the same order as, if not lower than, the control MII egg matured without DOA (0.83×10^7 ph.e$^-$/s; Fig. 3E). In contrast, culturing DOA-matured eggs alongside inhibition of β-oxidation with 100 µM Etomoxir for ∼6 h prior to CARS imaging (Fig. 4G-I) shows CD_2 and CH_2 CARS intensities similar to those seen immediately after maturation (time 0, Fig. 3B). These data are summarised in Table 1.

To better quantify these results, the average DOA volume per LD ($\langle v \rangle$) was calculated (see Materials and Methods) for all eggs under each condition described. Results were then plotted to quantitatively compare the loss of DOA signal after alteration of β-oxidation (Fig. 5). Carbohydrate starvation causes a significant loss of the DOA label (pink triangle), to levels that are comparable to those of control eggs matured without DOA (green diamond). Incubation with Etomoxir causes little or no decrease in the CARS signal (red circle) compared to that seen in control eggs imaged immediately after DOA maturation of eggs in the presence of DOA (black square). After ∼6 h incubation in simple M2 medium, eggs appear to lose the DOA label, demonstrating physiological fatty acid turnover (blue triangle); but this is not significantly different to control eggs. These data show that loss of DOA from LDs can be imaged in mouse eggs in a way that is consistent with endogenous β-oxidation. This, in turn, implies β-oxidation is enhanced during carbohydrate starvation. These data are summarised in Table 1.

Contribution of β-oxidation to the mitochondrial redox potential

The above data suggest that mouse eggs switch to using β-oxidation from endogenous fatty acid stores when pyruvate is not available. However, it is unclear how much β-oxidation is contributing to the overall mitochondrial metabolism of the egg in normal (M2) medium.

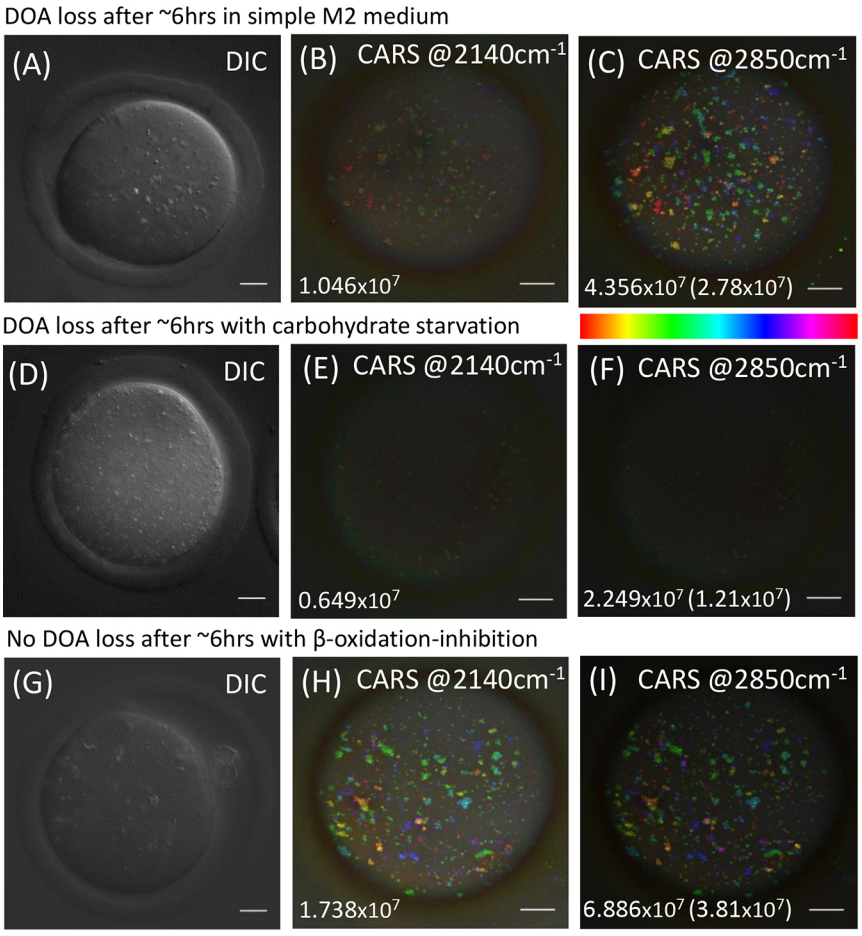

Fig. 4. Loss of DOA in eggs with altered mitochondrial metabolism. (A,D,G) Single-plane (approximately equatorial) DIC images using a 1.27 NA water objective and a 0.72 NA dry condenser. (B,C,E,F, H,I) Images show depth colour-coded CARS *z*-stacks at wavenumbers 2140 cm^{-1} (CD_2 vibration) (B,E,H) and 2850 cm^{-1} (CH_2 vibration) (C,F,I) through the same MII eggs. DOA in LDs is shown after 6 h in a representative egg incubated in simple M2 medium (n=4; A-C), in a carbohydrate-starved egg (n=8; D-F), in a β-oxidation-inhibited (100 µM Etomoxir) egg (n=6; G-I). Maximum CARS intensities are shown in photoelectrons per second (ph.e$^-$/s). Values in parenthesis in C, F and I denote the intensity under excitation conditions identical to those in B,E and H, respectively, i.e. they are corrected for the varying temporal overlap of pump and Stokes at different wavenumbers. Depth colour-coded CARS images shown in B, E and H were adjusted to the brightness of that shown in H; depth colour-coded CARS images shown in C, F and I were adjusted to the brightness of that shown in I. *xy* pixel size, 0.1×0.1 µm; *z*-step, 0.5 µm; pixel dwell time, 0.01 ms; Pump (Stokes) power at the sample, ∼14 mW (∼9 mW). Scale bars: 10 µm. Colour bar shows depth of colour coding, ranging from −25 µm to 25 µm of 101 *z*-stacks, with 0 µm being the approximate equatorial plane of the egg. Data represent multiple trials, using two to three mice per trial.

Journal of Cell Science (2019) 132, jcs228999. doi:10.1242/jcs.228999

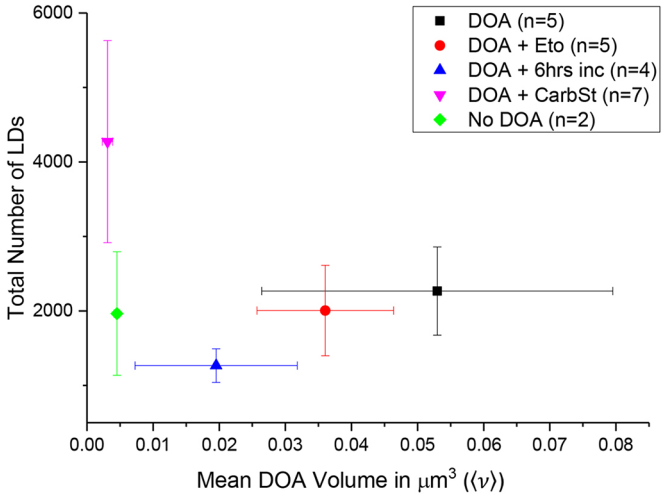

Fig. 5. DOA content of eggs with altered mitochondrial metabolism. Mean DOA lipid volume in μm³ (‹v›) against total number of LDs in ensembles of control MII eggs imaged immediately after overnight incubation with DOA (black square, *n*=5), MII eggs incubated in Etomoxir for 6 h after incubation with DOA (red circle, *n*=5), MII eggs incubated in M2 medium for 6 h after incubation with DOA (blue triangle, *n*=4), carbohydrate-starved MII eggs, i.e. incubated in pyruvate-, lactate- and glutamine-free medium for 6 h after incubation with DOA (pink inverted triangle, *n*=7), and MII eggs incubated in M2 medium without DOA (green diamond, *n*=2). The distribution of each variable in the corresponding ensemble is shown as the average±s.e.m. Data represent multiple trials, using two to three mice per trial.

FAD autofluorescence can be used as a measure of the redox state of mitochondria within eggs (Dumollard et al., 2004). Addition of 100 μM Etomoxir to inhibit β-oxidation in mouse eggs caused a marked decrease in FAD signal (Fig. 6A), with a slight oscillation before settling to a new, more-reduced FAD level. The redox state of FAD in mitochondria can be calibrated by the addition of cyanide (CN^-) and FCCP. Addition of 2 mM CN^- prevents the reduction of oxygen in the electron transport chain (ETC), inducing a maximally reduced ($FADH_2$) redox state (Fig. 6B), whereas addition of 1 μM FCCP uncouples mitochondrial oxidative phosphorylation, after perfusion of fresh medium, causes maximum oxidation (Fig. 6C). This calibration of the FAD autofluorescence signal allows the contribution of fatty acid oxidation to be assessed. By comparing the starting value of the FAD fluorescence with the maximal and minimum fluorescence values obtained by using CN^- and FCCP, respectively, we estimated the MII mouse egg mitochondria to be at 60.5±3.1% (mean ±s.e.m.) of their total redox potential. In addition, from the change in FAD fluorescence induced by Etomoxir we estimated that β-oxidation contributes 49.8±2.7% of the starting or 'resting' mitochondrial FAD/$FADH_2$ redox state. It should be noted that the effects of Etomoxir were specific to mitochondrial flavoproteins because addition of Etomoxir after FCCP or CN^- treatment of eggs causes no change in autofluorescence (Fig. S2).

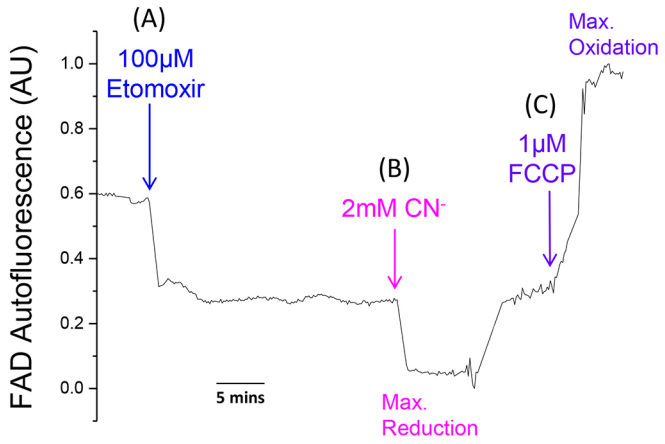

Fig. 6. FAD Autofluorescence imaging of the mitochondrial redox potential. Mitochondrial FAD autofluorescence signal in MII eggs subjected to (A) β-oxidation inhibition (100 μM Etomoxir) followed by (B) induction of maximum reduction (2 mM cyanide) followed by (C) subsequent maximum oxidation (1 μM FCCP) after performing a perfusion washing step. Data represent multiple eggs (*n*=15), using two to three mice trials.

Contribution of β-oxidation and pyruvate metabolism to ATP production

The FAD:$FADH_2$ ratio in mitochondria gives an indication of mitochondrial metabolism but we also wanted to examine the immediate effect on ATP production of interfering in β-oxidation. To monitor the relative ATP levels in eggs we microinjected firefly luciferase and the luminescence was measured in eggs incubated in HKSOM containing 100 μM luciferin (Dumollard et al., 2008). Inhibition of β-oxidation following addition of 100 μM Etomoxir during imaging caused a transient decrease in luminescence, luminescence recovered to levels similar to those seen at the start of recording (Fig. 7A). This suggests that eggs require β-oxidation to maintain ATP levels but also that they can rapidly compensate for reduced β-oxidation to restore previous resting ATP. Mitochondrial pyruvate uptake can be inhibited in mouse eggs by addition of 500 μM cinnamate during imaging. We found that this also leads to a decrease in the production of ATP [Fig. 7B(i)]. However, the subsequent inhibition of β-oxidation with Etomoxir led to a further ATP decrease that, interestingly, does not recover – as seen following addition of Etomoxir without prior pyruvate starvation [Fig. 7B(ii)]. These data suggest that pyruvate uptake is required for eggs to maintain ATP levels in the absence of β-oxidation. From the size of the relative changes in luciferase luminescence it also appears that ∼50% of the resting ATP in an MII egg is attributable to β-oxidation.

A conventional luminescent assay of whole-cell ATP was also performed in mouse eggs by lysing eggs in buffer and measuring luminescence in a luminometer. The luminescence signal emitted by eggs was calibrated with recombinant firefly luciferase to provide a certain amount of ATP per egg. We found that a control MII mouse egg has ∼3.5 mM ATP [Fig. 7C(i)]. Inhibition of β-oxidation with 100 μM Etomoxir did not appear to change the whole-cell ATP after incubation for 1 hour [Fig. 7C(ii)], neither did 1-h starvation of pyruvate following addition of 500 μM cinnamate or incubation in medium lacking pyruvate, lactate, glucose and glutamine [Fig. 7C(iii)]. However, incubation of eggs and simultaneous inhibition of β-oxidation and starvation of carbohydrates dramatically decreased the amount of ATP seen in whole cells after 1 h [Fig. 7C (iv)]. Incubation with 1 μM FCCP demonstrated the lowest amount of ATP reached [Fig. 7C(v)]. These data are consistent with the results seen with the dynamic luciferase assay of ATP shown in Fig. 7A,B, in that only the combined inhibition of pyruvate and fatty acid oxidation by mitochondria led to a significant decrease in ATP in mouse eggs. The data support the idea that pyruvate uptake can compensate for loss of β-oxidation in the generation of ATP.

DISCUSSION

It is widely accepted that pyruvate is the principal mitochondrial substrate for mouse or human eggs (Dumollard et al., 2009).

Journal of Cell Science (2019) 132, jcs228999. doi:10.1242/jcs.228999

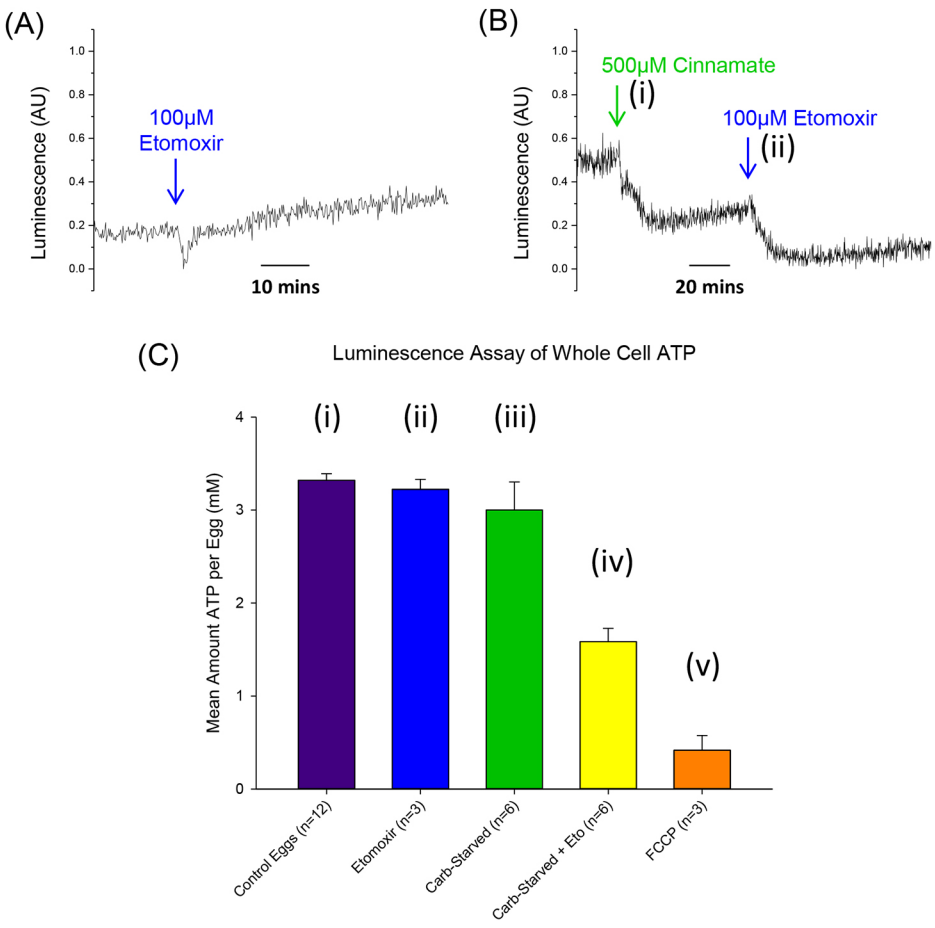

Fig. 7. Luminescence imaging of ATP in cells with altered mitochondrial metabolism. (A,B) Live-cell luciferase imaging of the change in ATP production in response to (A) inhibition of β-oxidation (100 μM Etomoxir; *n*=12) or (B) inhibition of pyruvate uptake (500 μM cinnamate) followed by that of β-oxidation (100 μM Etomoxir; *n*=13). (C) Histogram of average whole-cell ATP measurements in ensembles of MII eggs. (i) Incubation in simple M2 medium (Control; *n*=12), (ii) inhibition of β-oxidation (100 μM Etomoxir) (*n*=3), (iii) inhibition of pyruvate-uptake (starvation medium or treatment with 500 μM cinnamate) (Carb-Starved; *n*=6), (iv) inhibition of pyruvate-uptake followed by inhibition of β-oxidation (modified incubation medium and 100 μM Etomoxir or treatment with 500 μM cinnamate and 100 μM Etomoxir) (Carb-Starved+Eto; *n*=6), (v) uncoupling of mitochondrial oxidative phosphorylation with 1 μM FCCP (*n*=3). Luminescence measurements were taken after 1 h of treatment. Data are +s.e.m. (*n*=number of eggs) from multiple trials, using two to three mice per trial.

However, in recent years it has become clear that mitochondrial fatty acid oxidation in mouse eggs and early embryos is also important, affecting their developmental viability (Dunning et al., 2010, 2011). Here, we showed that LDs change their spatial distribution when carbohydrates are unavailable, and that we can image the metabolism of fatty acids in LDs within live eggs by using CARS microscopy and deuterium-labelled fatty acids. We also provided evidence that β-oxidation provides a substantial contribution to both the ATP output, and the resting redox state of the MII mouse egg.

The metabolic state of the mammalian egg or embryo is indicative of its developmental potential (Leese, 2002; Leese et al., 2016). We have now found that the level of β-oxidation occurring in the egg is reflected in its LD distribution. It appears that when the LDs are in a distinctly clustered arrangement, fatty acid oxidation is decreased, while pyruvate oxidation is likely to be dominant. By contrast, LDs – which are widely dispersed throughout the cytoplasm – signify an increased capacity for β-oxidation, where pyruvate may be limited. LDs are likely to be disperse in order to increase the surface area available for fatty acid mobilisation, while clustering may be indicative of energy conservation. Moreover, it might be that these eventually coalesce into larger LDs, as seen at the morula and blastocyst stages of later pre-implantation embryo development (Bradley et al., 2016). It is notable that, although a number of proteins involved in LD fusion have been described, the mechanism of clustering that might act as a prelude to fusion, has not been established (Walther and Farese, 2012).

Deuterium labelling of LDs by using the ability of the cell to incorporate DOA has allowed dynamic visualisation of fatty acid turnover. Oleic acid has been shown to promote the formation of TAGs and lipid storage as LDs in eggs (Zhang et al., 2011; Shaaker et al., 2012), and was, thus, chosen as the perfect candidate to introduce a detectable deuterium signal to LDs. We have shown that DOA is readily taken up into LDs and can be clearly observed, also resulting in a reduction of the endogenous lipid signal within the cell (Fig. 3C versus F, Table 1). Notably, since DOA is fully deuterated, the observation of a significant CARS intensity at the CH_2 peak in many droplets that exhibit CARS signals at the CD_2 resonance suggests that DOA is incorporated into LDs as TAGs containing a combination of fatty acids rather than pure DOA (Figs 3C, 4I and Fig. S1). It is also evident that fatty acids are readily liberated from LDs for oxidation within the mitochondria, demonstrated by the loss of this label over time (Figs 4B and 5, blue triangle). We clearly observe that carbohydrate starvation almost removes the CD_2 signal while greatly reducing the CH_2 signal (Fig. 4E,F; Fig. 5, pink triangle), indicating global fatty acid metabolism in the compensatory response. It should be noticed that the loss of label occurred in eggs that were either carbohydrate-deprived or kept in control (M2) medium. Hence, even if eggs can take up pyruvate – as well as short-chained fatty acids – from medium, they are still active in oxidising fatty acid from LD stores under resting conditions.

When we blocked β-oxidation in eggs by adding Etomoxir, it was surprising to observe a distinct decrease in the autofluorescent FAD signal (Fig. 6A). Such decrease in FAD reflects a shift to the generation of a more-reduced redox state when $FADH_2$ is formed (Duchen, 2000). This type of shift has been seen before in mouse egg mitochondria, in response to sperm-induced Ca^{2+} increases, which increase pyruvate oxidation (Dumollard et al., 2004). We also found that a similar decrease in autofluorescence occurs when eggs are exposed to high levels of pyruvate and dichloroacetate, which

Journal of Cell Science (2019) 132, jcs228999. doi:10.1242/jcs.228999

promotes pyruvate oxidation (Fig. S3). This is consistent with the finding that most of the FAD autofluorescence in mitochondria originates from lipoamide dehydrogenase, which is part of the pyruvate dehydrogenase complex (Kunz and Kunz, 1985). Hence, our data suggest that blockage of fatty acid oxidation leads to an almost immediate increase in oxidation of pyruvate, to compensate for the loss of fatty acid oxidation.

A compensatory increase in pyruvate oxidation could explain why Etomoxir caused only a brief and transient decrease in ATP levels before they recovered to one similar to ATP resting level. Luminescence ATP measurements provided more insight as to the identity of this alternative substrate, since inhibition of mitochondrial pyruvate uptake in response to a cinnamate derivate prevented the recovery of ATP levels after Etomoxir addition [Fig. 7B,C(iv)]. This clearly suggests that a compensatory increase in pyruvate uptake is responsible for the recovery of ATP levels and the decrease in FAD autofluorescence signals seen with removal of fatty acid oxidation. Whole-cell ATP measurements lack the dynamic resolution but still support the live-cell luciferase measurements since a significant decrease in ATP content was only seen when using a combination of both Etomoxir and cinnamate to block both fatty acid and pyruvate oxidation. It is notable that changes in FAD fluorescence or live-cell ATP measurements – in the presence of cinnamate – were both substantial, representing∼40% of the total signal that can be attributed to mitochondrial function. Hence, these data suggest that, within mouse eggs, mitochondrial oxidation of pyruvate and fatty acids is in a reciprocal balance with fatty acids that contribute half of the energy required for ATP generation under resting conditions. This balance resembles the Randle cycle, as described for the reciprocal balance between fatty acid and glucose oxidation in somatic cells (Randle et al., 1963). The egg and early embryo variant of the Randle cycle would be between fatty acids and pyruvate, with the control point presumably exerted by levels of acetyl-CoA inside mitochondria.

There is previous evidence for a reciprocal balance between pyruvate and fatty acid oxidation in mouse eggs or early embryos. For example, Etomoxir inhibition of β-oxidation causes an increase in activity of the pyruvate dehydrogenase (PDH) complex (Bryson et al., 1996). O_2 consumption also continues in the absence of pyruvate (Butcher et al., 1998). Interestingly, it has also been shown in skeletal muscle and hepatocytes that inhibition of the TC protein complex I – accepting electrons directly from PDH complex-derived NADH – causes an increase in β-oxidation and mobilisation of TAGs from LD storage (Collier et al., 2006; Owen et al., 2000).

Neither pyruvate nor fatty acids appear to be optimal for early embryo development. Previous studies that used Etomoxir have proven that β-oxidation is required (Dunning et al., 2010; Downs et al., 2009; Merrill et al., 2002), whereas egg pyruvate-starvation has been shown to result in reduced fertilisation and a reduction in ATP (Dumollard et al., 2004; Collado-Fernandez et al., 2012). It is also clear that excessive pyruvate or fatty acid oxidation leads to excessive production of ROS (Dumollard et al., 2009). It is possible that a 'balanced diet' of pyruvate and β-oxidation helps to maintain a low level of metabolism of each substrate, such that the overall metabolic activity of the egg is kept low. This is in accordance with the 'quiet embryo hypothesis' (also known as 'Goldilocks principle'), which states that the optimal level of metabolism within the developing egg or embryo is 'just right', i.e. neither too low to compromise development, nor too high to result in overproduction of ROS (Leese et al., 2016). We propose that low levels of both pyruvate and fatty acid oxidation are maintained to reduce excess ROS generated under conditions of high metabolic activity.

Together, our data demonstrate that mitochondrial pyruvate and fatty acid oxidation in mouse eggs are in balance, and able to compensate for loss of the other. It is clear that β-oxidation contributes substantially to the mitochondrial production of ATP; however, it appears that it is not crucial in maintaining ATP levels. This suggests that β-oxidation has an alternative important role in development. We also show that fatty acid turnover can be imaged in live cells by using a unique microscopy method that is compatible with egg and embryo viability (Bradley et al., 2016). Thus, it is possible to correlate LD distribution with the pattern of metabolism or developmental potential of eggs and early embryos.

MATERIALS AND METHODS

Gamete collection and culture

Female MF1 (4-6 weeks old) or CD1 (8 weeks old) mice were intraperitoneally injected with 5IU of pregnant mare's serum gonadotrophin (PMSG) to induce ovarian follicle development. They were again injected with 10IU human chorionic gonadotrophin (hCG) ∼48 h later to induce ovulation. Ovulated mature metaphase II-arrested (MII) eggs were collected from oviducts ∼15 h later. Immature germinal vesicle (GV) stage eggs for *in vitro* maturation (IVM) were collected from the punctured ovarian follicles of non-injected mice. Cumulus cells were removed by gentle pipetting (for GV oocytes) or brief exposure to hyaluronidase (for MII oocytes). All animals were handled according to UK Home Office regulations, and procedures carried out under a UK Home Office Project License with approval by Cardiff University Animal Ethics Committee. Data shown are from experiments using eggs from MF1 mice, except for data shown Figs S2 and S3, for which eggs from CD1 mice were used.

All eggs were kept in drops of M2 medium (embryo tested, Sigma) at 37°C. β-oxidation was inhibited in MII eggs following the addition of Etomoxir (Sigma) to M2 medium and culturing for ∼6 h prior to imaging. Carbohydrate starvation was carried out by incubating MII eggs in HEPES-buffered potassium-supplemented simplex optimised medium (HKSOM) containing 3 mg/ml bovine serum albumin (BSA, both Sigma) lacking pyruvate, lactate, glutamine, and glucose, also for ∼6 h prior to imaging. To assess storage and use of fatty acids within the mammalian egg, deuterated oleic acid (DOA) (oleic acid-d_{34}, Sigma) bound to fatty acid-free BSA (Sigma) was introduced to eggs during IVM of GV eggs through incubation in Minimum Essential Medium (MEM, Sigma) containing 400 µM DOA and 3 mg/ml BSA for ∼18 h overnight. All drops were covered with mineral oil (embryo tested, Sigma) to prevent evaporation.

CARS and DIC microscopy

Live eggs were pipetted into a drop of M2 medium in an in-house-built imaging dish consisting of a 25 mm diameter glass coverslip and a removable glass lid. The drop of M2 medium was maintained at 37°C and covered in oil to prevent evaporation. The CARS microscope was set up as described by Pope et al. (2013), with DIC imaging capabilities. Briefly, CARS excitation fields were obtained by spectrally separating broadband 5 fs laser pulses with an appropriate sequence of dichroic beam splitters, resulting in a pump (Stokes) beam with centre wavelength of 682 nm (806 nm) and a bandwidth of 65 nm (200 nm). Spectral focusing through linear chirping of the pump and Stokes fields resulted in pulse durations of ∼1 ps and ∼4 ps, respectively, achieving a high spectral resolution of 10 cm^{-1}. The excitation pulses were recombined and directed via a home-built beam-scanning head into a Nikon Ti-U inverted microscope. A 1.27 NA ×60 water immersion objective (Nikon λS series) and a 0.72 NA dry condenser equipped with DIC optics were used, providing high spatial resolution (0.3 µm lateral, 0.6 µm axial as CARS intensity point-spread function) and forward-CARS collection efficiency.

A monochrome ORCA-285 Hamamatsu CCD camera was used for DIC imaging. A motorised sample stage enabled lateral *xy* sample movement, and axial *z* movement for focussing was enabled by a motorised *z*-drive (Prior ProScan III). CARS at the anti-Stokes frequency was selected by an appropriate band-pass filter (Semrock) and detected by a photomultiplier tube (Hamamatsu H7422-40). For non-deuterated samples, filters transmitting

light at wavelengths between 542 and 582 nm (allowing detection of wavenumbers in the range of 3787–2519 cm^{-1}) were used to detect the CARS signal from the CH_2 stretch resonance (data presented in Fig. 2). When imaging deuterated samples filters transmitting light in the range of 573–613 nm (allowing detection of wavenumbers in the range of 2950 cm^{-1} to 1650 cm^{-1}) were used. This second filter set (although not optimised for the CH_2 resonance) allowed sequential single-frequency CARS images to be obtained at the CARS peaks of both the CD_2 (2140 cm^{-1}) and CH_2 (2850 cm^{-1}) stretch vibration resonances (data presented in Figs 3-5).

3D *z*-stacks of CARS images were taken over a 50 µm depth of the egg in 0.5 µm steps, from −25 µm to +25 µm (0 µm being approximately equatorial). CARS images in *xy* were taken at 0.1 µm pixel size, typically in an 80×80 µm frame, with a pixel dwell time of 0.01 ms and time-average total power of ∼20 mW at the sample. MultiCARS software (in-house developed) allowed collection and regularisation of images from the CARS microscope. Image stacks were assembled into maximum intensity projections and depth colour-coded projections by using ImageJ.

As mentioned above, single-frequency CARS images were obtained by exciting and detecting at the CD_2 and CH_2 stretch vibrational resonances of 2140 cm^{-1} and 2850 cm^{-1}, respectively. To directly compare the measured CARS intensities, one must correct for differences in the excitation and detection efficiencies at these two wavenumbers. In particular, the temporal overlap of the exciting pump and Stokes beams is different, since wavenumber tuning in our set-up occurs through changing the delay time between pump and Stokes, as described in Pope et al. (2013). Glass has a spectrally constant non-resonant CARS response (susceptibility) in this wavenumber range, therefore any variation in the intensity of the CARS signal measured in the glass at different wavenumbers is due to differences in the excitation and detection efficiencies. This property can be used to correct the measured CARS intensities in the following way. The CARS intensity from glass is measured under the same excitation and detection conditions as those used to measure the images of the egg at the CD_2 and CH_2 stretch vibrational resonances. The CARS intensity from the image of the egg taken at the CH_2 stretch resonance I_{2850} is then multiplied by the ratio of the two intensities measured in glass G_{2140}/G_{2850} to obtain the corrected intensity $(I_{2850})_{CR}$ for direct comparison with the values measured at the CD_2 i.e. $(I_{2850})_{CR} = I_{2850}(G_{2140}/G_{2850})$, where G_{2140} and G_{2850} are the CARS intensities measured in the glass at the CD_2 and CH_2 wavenumbers, respectively.

3D *z*-stacks of DIC images were taken over the full depth of the egg (∼70 µm) in 0.5 µm steps, with 20 ms frame exposure time, using the MicroManager software. A polarisation angle of 12.5° in the de-Senarmont DIC illuminator yields a 25° phase offset that was found to be sufficiently small to enable good image contrast and sufficiently high to enable quantitative analysis of small phase objects, such as lipid membranes (McPhee et al., 2013).

LD aggregate analysis

The in-house-developed CCDPlot software allowed detection of the 3D coordinates, *x*,*y*,*z* widths and amplitude peaks of LDs from single-frequency CARS images, as described by Bradley et al. (2016). By using these coordinates, 'clusters' were defined when the LD centre spatial position was within a distance of 1.5× the resolution (0.3 µm laterally, 0.6 µm axially) to that of the nearest neighbouring droplet (Fig. 2J; Bradley et al. 2016). To compare mean aggregate sizes across different developmental stages, the probability P_k of each size k=1, 2, 3, etc. (including size 1, i.e. isolated LDs) was calculated from the histogram (Fig. 2G,H) of the aggregate size by using P_k=O_k/N, where N is the total number of LDs and O_k is the occurrence of size k. The mean square size was then calculated as $\langle s^2 \rangle = \sum_{k=1}^{+\infty} (k-1)^2 P_k$ for each egg (where we subtracted 1 to obtain the number of partner LDs in an aggregate). Origin software (OriginLab) was used to plot the square root of the mean square aggregate size (i.e. $\sqrt{\langle s^2 \rangle}$) for all eggs under an experimental condition against their total number of LDs.

Analysis of DOA volume within LDs

To calculate the average DOA lipid volume in μm^3 per LD, we first determined the LD volume by multiplying the LD widths in *x*, *y*, *z* as obtained from CCDPlot analysis. The amplitude of the CARS signal at 2140 cm^{-1} obtained for each LD (A_i, square root of the CARS intensity) was normalised to a constant amplitude of the brightest droplet in a control DOA egg (A_b) using A_i/A_b, to define relative DOA densities and compare lipid volumes across conditions. The normalised LD amplitude was then multiplied by the LD volume to calculate the normalised DOA lipid volume per LD.

To compare the average DOA volume per LD across different conditions, the probability (P_{Vi}) of each DOA volume (v_i) was calculated from the histogram of the normalised DOA volumes. We used P_{vi}=O_{vi}/O, where $O = \sum_{vi}^{O}$ and O_{vi} is the occurrence of volume v_i. The mean volume was then calculated as $\langle v \rangle = \sum (v_i\, P_{vi})$ for each egg. Origin was used to plot the $\langle v \rangle$ for all eggs under an experimental condition, against their total number of LDs.

FAD autofluorescence assay of redox potential

Epifluorescence measurements of FAD autofluorescence were performed using a Nikon Ti-U microscope. Excitation light was provided by a halogen lamp and a Photometrics CoolSnap HQ2 CCD camera was used to collect fluorescence data. A 460 nm excitation filter (10 nm bandpass) and 510–550 nm emission filter were used, alongside a 505 nm dichroic mirror. Eggs were briefly exposed to acid Tyrode's solution (Sigma) to remove the zona pellucida, allowing them to stick to the microscope dish, to minimise disturbance during addition of experimental chemical treatments to the surrounding medium. A perfusion apparatus was set up to replace imaging medium with fresh medium throughout experiments requiring addition of multiple drugs with opposing mechanisms. InVivo software was used to collect data, ImageJ was used to collect data per egg using the MultiMeasure Plug-in, when selecting regions of interest. SigmaPlot and Origin were used for normalisation and plotting of data. Graphs were normalised by: $\frac{x_0 - x_{min}}{x_{max} - x_{min}}$ where x_0 is the resting fluorescence level before drug addition, and x_{min} and x_{max} are the minimum and maximum fluorescence levels reached, respectively. This allowed calculation of the contribution of β-oxidation to the redox potential. The intensity of fluorescence emission is presented in arbitrary units.

Luminescence assays of ATP

A live-cell luciferase assay of ATP was performed by microinjecting MII eggs with firefly luciferase protein (10 µg/ml). Injections were performed within a shallow drop of M2 medium under mineral oil to prevent evaporation, upon an unheated microscope stage (Nikon TE2000). Injection needles were pulled on a vertical puller (P-30, Sutter Instruments) and connected to an intracellular amplifier (Cyto721, WPI). A Picopump (WPI Ltd) operated by a foot pump was used to provide a short pressure pulse of ∼20 psi, to introduce a small amount of luciferase to the egg (∼3-5% its volume). Eggs were then pipetted into HKSOM containing 100 µM luciferin, under mineral oil, on the heated stage of a Zeiss Axiovert S100 microscope within a purpose-built dark box. Photek software was used to collect data per ROI; Origin was used for normalisation and plotting of data. Graphs were normalised by: $\frac{x_0 - x_{min}}{x_{max} - x_{min}}$ as described above. The luminescence values in experiments represent the absolute number of measured photon counts per 10 s.

Whole-cell assays to analyse ATP levels were performed by pipetting individual whole eggs into 200 µl CellTiter-Glo® Luminescent Cell Viability Assay reagent (Promega) before measuring the resultant luminescence signal in a home-built luminometer for 5 min. Luminescence signals were collected by a cooled S20 photomultiplier tube (Electron Tubes Ltd., UK). The data were collected and plotted using the Electron Tubes RS232 Photon Counting software, enabling subsequent SigmaPlot analysis. A calibration curve was produced using increasing known concentrations of ATP (1 fmol-10 pmol) within the same volume of reagent and was used to determine the total amount of ATP per egg (mM values in a 200-pl egg). SigmaPlot software was used to plot the mean total ATP per ensemble of eggs +s.e.ms.

Chemical treatments

Chemical treatments were added to HKSOM during luminescence and epifluorescence imaging, while eggs were incubated in different drug

combinations for ∼1 h prior to taking whole-cell ATP measurements. Etomoxir (Sigma) was added at 100 µM final concentration to inhibit β-oxidation. Alpha cyano-4 hydroxycinnamate (referred to as cinnamate, Sigma) was added at a final concentration of 0.5 mM, to prevent pyruvate transport into mitochondria. 2 mM sodium cyanide (CN^-, Sigma) was used to induce a fully reduced redox state, while the uncoupler carbonyl cyanide-4-(trifluoromethoxy)phenylhydrazone (FCCP; Sigma) was added to medium at a final concentration of 1 µM for a fully oxidised redox state. Perfusion of medium in the microscope dish with fresh medium throughout measurements allowed subsequent addition of CN^- and FCCP within the same experiment.

Acknowledgements
The authors thank Dale Boorman for provision of deuterated and non-DOA Raman spectra, and Ros John for advice and discussions.

Competing interests
The authors declare no competing or financial interests.

Author contributions
Conceptualization: J.B., W.L., P.B., K.S.; Methodology: J.B., I.P., W.L., P.B., K.S.; Software: W.L., P.B.; Validation: I.P., W.L., P.B.; Formal analysis: J.B., I.P., Y.W.; Investigation: J.B., I.P., Y.W., K.S.; Resources: W.L., K.S.; Data curation: J.B., Y.W., P.B.; Writing - original draft: J.B., K.S.; Writing - review & editing: J.B., I.P., W.L., P.B., K.S.; Supervision: W.L., P.B., K.S.; Project administration: P.B., K.S.; Funding acquisition: W.L., P.B., K.S.

Funding
J.B. acknowledges financial support by the President's Research Scholarship programme of Cardiff University and the UK Biotechnology and Biological Sciences Research Council (BBSRC) responsive mode research grant (grant no. BB/P007511/1). P.B. acknowledges the UK Engineering and Physical Sciences Research Council (EPSRC) for her Leadership fellowship award (grant no. EP/I005072/1) and the Royal Society for her Wolfson Research Merit Award (grant no. WM140077). I.P. is funded by the UK EPSRC (grant no. EP/L001470/1) and UK BBSRC (grant no. BB/P007511/1). W.L. acknowledges support by a Royal Society Leverhulme Research Fellowship (grant no. LT20085). The CARS microscope set-up was funded by the UK BBSRC [grant nos BB/H006575/1 and BB/P007511/1].

Data availability
Data access information about the data created during this research, including how to access it, is available from Cardiff University data archive at http://doi.org/10.17035/d.2019.0078592340

Supplementary information
Supplementary information available online at
http://jcs.biologists.org/lookup/doi/10.1242/jcs.228999.supplemental

References
Apparicio, M., Ferreira, C. R., Tata, A., Santos, V. G., Alves, A. E., Mostachio, G. Q., Pires-Butler, E. A., Motheo, T. F., Padilha, L. C., Pilau, E. J. et al. (2012). Chemical composition of lipids present in cat and dog egg by matrix-assisted desorption ionization mass spectrometry (MALDI-MS) *Reprod. Dom. Anim.* **47**, 113-117. doi:10.1111/rda.12003

Bergner, G. Albert, C. R., Schiller, M., Bringmann, G., Schirmeister, T., Dietzek, B., Niebling, S., Schlucker, S. and Popp, J. (2011). Quantitative detection of C-deuterated drugs by CARS microscopy and Raman microspectroscopy. *Analyst* **136**, 3686-3693. doi:10.1039/c0an00956c

Bradley, J. (2016). Label-free multiphoton microscopy of lipid droplets in oocytes, eggs, and early embryos. *PhD Thesis*, Cardiff University.

Bradley, J., Pope, I., Masia, F., Sanusi, R., Langbein, W., Swann, K. and Borri, P. (2016). Quantitative imaging of lipids in live mouse eggsand early embryos using CARS microscopy. *Development* **143**, 2238-2247. doi:10.1242/dev.129908

Bryson, J. M., Cooney, G. J., Wensley, V. R., Phuyal, J. L. and Caterson, I. D. (1996). The effects of the inhibition of fatty acid oxidation on pyruvate dehydrogenase complex activity in tissues of lean and obese mice. *Int. J. Obes. Relat. Metab. Disord.* **20**, 738-744.

Butcher, L., Coates, A., Martin, K. L., Rutherford, A. J. and Leese, H. J. (1998). Metabolism of pyruvate in the early human embryo. *Biol. Reprod.* **58**, 1054-1056. doi:10.1095/biolreprod58.4.1054

Collado-Fernandez, E., Picton, H. and Dumollard, R. (2012). Metabolism throughout follicle and egg development in mammals. *Int. J. Dev. Biol.* **56**, 799-808. doi:10.1387/ijdb.120140ec

Collier, C. A., Bruce, C. R., Smith, A. C., Lopschuk, G. and Dyck, D. J. (2006). metformin counters the insulin-induced suppression of fatty acid oxidation and stimulation of triglycerol storage in rodent skeletal muscle. *Am. J. Physiol. Endocrinol. Metab.* **291**, 182-189. doi:10.1152/ajpendo.00272.2005

Downs, S. M. (1995). The influence of glucose, cumulus cells and metabolic coupling on ATP levels and meiotic control in the isolated mouse egg. *Dev. Biol.* **167**, 502-512. doi:10.1006/dbio.1995.1044

Downs, S. M., Mosey, J. L. and Klinger, J. (2009). Fatty acid oxidation and meiotic resumption in mouse eggs. *Mol. Reprod. Dev.* **76**, 844-853. doi:10.1002/mrd.21047

Duchen, M. R. (2000). Mitochondria and calcium: from cell signalling to cell death. *J. Physiol.* **529**, 57-68. doi:10.1111/j.1469-7793.2000.00057.x

Dumollard, R., Marangos, P., Fitzharris, G., Swann, K., Duchen, M. and Carroll, J. (2004). Sperm-triggered [Ca^{2+}] oscillations and Ca2+ homeostasis in the mouse egg have an absolute requirement for mitochondrial ATP production. *Development* **131**, 3057-3067. doi:10.1242/dev.01181

Dumollard, R., Ward, Z., Carroll, J. and Duchen, M. (2007). Regulation of redox metabolism in the mouse egg and embryo. *Development* **134**, 455-465. doi:10.1242/dev.02744

Dumollard, R., Campbell, K., Halet, G., Carroll, J. and Swann, K. (2008). Regulation of cytosolic and mitochondrial ATP levels in mouse eggs and zygotes. *Dev. Biol.* **316**, 431-440. doi:10.1016/j.ydbio.2008.02.004

Dumollard, R., Carroll, J., Duchen, M. R., Campbell, K. and Swann, K. (2009). Mitochondrial function and redox state in mammalian embryos. *Semin. Cell. Dev. Biol.* **20**, 346-353. doi:10.1016/j.semcdb.2008.12.013

Duncan, M. D., Reintjes, J. and Manuccia, T. J. (1982). Scanning coherent anti-stokes raman microscope. *Opt. Lett.* **7**, 350-352. doi:10.1364/OL.7.000350

Dunning, K. R., Cashman, K., Russell, D. L., Thompson, J. G., Norman, R. J. and Robker, R. L. (2010). Beta-oxidation is essential for mouse egg developmental competence and early embryo development. *Biol. Reprod.* **83**, 909-918. doi:10.1095/biolreprod.110.084145

Dunning, K. R., Akison, L. K., Russell, D. L., Norman, R. J. and Robker, R. L. (2011). Increased beta-oxidation and improved egg developmental competence in response to L-carnitine during ovarian *in vitro* follicle development in mice. *Biol. Reprod.* **85**, 548-555. doi:10.1095/biolreprod.110.090415

Fu, D., Yu, Y., Folick, A., Currie, E., Farese, R. V., Jr, Tsai, T.-H., Xie, X. S. and Wang, M. C. (2014). In vivo metabolic fingerprinting of neutral lipids with hyperspectral stimulated Raman scattering microscopy. *J. Am. Chem. Soc.* **136**, 8820-8828. doi:10.1021/ja504199s

Gardner, D. K. and Leese, H. J. (1986). Non-invasive measurement of nutrient uptake by single cultured pre-implantation mouse embryos. *Hum. Reprod.* **1**, 25-27. doi:10.1093/oxfordjournals.humrep.a136336

Homa, S. T., Racowsky, C. and McGaughey, R. W. (1986). Lipid analysis of immature pig eggs. *J. Reprod. Fert.* **77**, 425-434. doi:10.1530/jrf.0.0770425

Kunz, W. S. and Kunz, W. (1985). Contribution of different enzymes to flavoprotein fluorescence of isolated rat liver mitochondria. *Biochem. Biophys. Acta* **841**, 237-246. doi:10.1016/0304-4165(85)90064-9

Leese, H. (2002). Quiet please, do not disturb: a hypothesis of embryo metabolism and viability. *BioEssays* **24**, 845-849. doi:10.1002/bies.10137

Leese, H. J., Guerif, F., Allgar, V., Brison, D., Lundin, K. and Sturmey, R. (2016). Biological optimization, the goldilocks principle, and how much is lagom in the preimplantation embryo. *Mol. Reprod. Dev.* **83**, 748-754. doi:10.1002/mrd.22684

McEvoy, T. G., Coull, G. D., Broadbent, P. J., Hutchinson, J. S. M. and Speake, B. K. (2000). Fatty acid composition of lipids in immature cattle, pig and sheep oocytes with intact zona pellucida. *J. Reprod. Fertil.* **118**, 163-170. doi:10.1530/jrf.0.1180163

McPhee, C. I., Zoriniants, G., Langbein, W. and Borri, P. (2013). Measuring the lamellarity of giant lipid vesicles with differential interference contrast microscopy. *Biophys. J.* **105**, 1414-1420. doi:10.1016/j.bpj.2013.07.048

Merrill, C. L., Ni, H., Yoon, L. W., Tirmenstein, M. A., Narayanan, P., Benavides, G. R., Easton, M. J., Creech, D. R., Hu, C. X., McFarland, D. C. et al. (2002). Etomoxir-Induced oxidative stress in HepG2 cells detected by differential gene expression is confirmed biochemically. *Toxicol. Sci.* **68**, 93-101. doi:10.1093/toxsci/68.1.93

Owen, M. R., Doran, E. and Halestrap, P. (2000). Evidence that metformin exerts its anti-diabetic effects through inhibition of complex I of the mitochondrial respiratory chain. *Biochem. J.* **348**, 607-614. doi:10.1042/bj3480607

Pope, I., Langbein, W., Watson, P. and Borri, P. (2013). Simultaneous hyperspectral differential-CARS, TPF, and SHG microscopy with a single 5fs Ti:Sa laser. *Opt. Express* **21**, 7096-7106. doi:10.1364/OE.21.007096

Potma, E. O. and Xie, X. S. (2004). CARS microscopy for biology and medicine. *Opt. Photonics News* **15**, 40-45. doi:10.1364/OPN.15.11.000040

Randle, P. J., Hales, C. N., Garland, P. B. and Newsholme, E. A. (1963). The glucose fatty-acid cycle: its role in insulin sensitivity and the metabolic disturbances of diabetes mellitus. *Lancet* **1**, 785-789. doi:10.1016/S0140-6736(63)91500-9

Rodriguez, L. G., Lockett, S. J. and Holtom, G. R. (2006). Coherent anti-stokes Raman scattering microscopy: a biological review. *Cytom. Part A* **69A**, 779-791. doi:10.1002/cyto.a.20299

Shaaker, M., Rahimipour, A., Nouri, M., Khanaki, K., Darabi, M., Farzadi, L., Shahnazi, V. and Mehdizadeh, A. (2012). Fatty acid composition of human follicular fluid phospholipids and fertilization rate in assisted reproductive techniques. *Iran. Biomed. J.* **16**, 162-168. doi:10.6091/ibj.1081.2012

Sturmey, R. G. and Leese, H. J. (2003). Energy metabolism in pig eggsand early embryos. *Reproduction* **126**, 197-204. doi:10.1530/rep.0.1260197

Walther, T. C. and Farese, R. V. (2012). Lipid droplets and cellular metabolism. *Ann. Rev. Biochem.* **81**, 687-714. doi:10.1146/annurev-biochem-061009-102430

Zhang, D., Slipchenko, M. N. and Cheng, J.-X. (2011). Highly sensitive vibrational imaging by femtosecond pulse stimulated raman loss. *J. Phys. Chem. Lett.* **2**, 1248-1253. doi:10.1021/jz200516n